PCCP

ROYAL SOCIETY OF CHEMISTRY

PAPER

View Article Online
View Journal | View Issue

Cite this: *Phys. Chem. Chem. Phys.*, 2024, **26**, 6277

A theoretical spectroscopy study of the photoluminescence properties of narrow band Eu^{2+}-doped phosphors containing multiple candidate doping centers. Prediction of an unprecedented narrow band red phosphor†

Rami Shafei,[ad] Philipp Jean Strobel,[c] Peter J. Schmidt,[c] Dimitrios Maganas,*[a] Wolfgang Schnick*[b] and Frank Neese*[a]

We have previously presented a computational protocol that is based on an embedded cluster model and operates in the framework of TD-DFT in conjunction with the excited state dynamics (ESD) approach. The protocol is able to predict the experimental absorption and emission spectral shapes of Eu^{2+}-doped phosphors. In this work, the applicability domain of the above protocol is expanded to Eu^{2+}-doped phosphors bearing multiple candidate Eu doping centers. It will be demonstrated that this protocol provides full control of the parameter space that describes the emission process. The stability of Eu doping at various centers is explored through local energy decomposition (LED) analysis of DLPNO-CCSD(T) energies. This enables further development of the understanding of the electronic structure of the targeted phosphors, the diverse interactions between Eu and the local environment, and their impact on Eu doping probability, and control of the emission properties. Hence, it can be employed to systematically improve deficiencies of existing phosphor materials, defined by the presence of various intensity emission bands at undesired frequencies, towards classes of candidate Eu^{2+}-doped phosphors with desired narrow band red emission. For this purpose, the chosen study set consists of three UCr_4C_4-based narrow-band phosphors, namely the known alkali lithosilicates $RbNa[Li_3SiO_4]_2:Eu^{2+}$ (RNLSO2), $RbNa_3[Li_3SiO_4]_4:Eu^{2+}$ (RNLSO) and their isotypic nitridolithoaluminate phosphors consisting of $CaBa[LiAl_3N_4]_2:Eu^{2+}$ (CBLA2) and the proposed $Ca_3Ba[LiAl_3N_4]_4:Eu^{2+}$ (CBLA), respectively. The theoretical analysis presented in this work led us to propose a modification of the CBLA2 phosphor that should have improved and unprecedented narrow band red emission properties. Finally, we believe that the analysis presented here is important for the future rational design of novel Eu^{2+}-doped phosphor materials, with a wide range of applications in science and technology.

Received 12th December 2023,
Accepted 15th January 2024

DOI: 10.1039/d3cp06039j

rsc.li/pccp

I. Introduction

Phosphor-converted white light-emitting diodes (pc-WLEDs) serve as the present generation light sources for illumination purposes.[2–5] LED phosphor materials continue to attract the interest of materials scientists in both academia and industry, with research and development focusing on concurrent improvements in efficiency and cost-effectiveness.[6,7] There are numerous applications in lighting and display backlighting technologies.[3,4,8–12] This is due to the capability of phosphors to produce high-quality light in the spectrum between far-red and blue wavelengths.[13–15] They are also environmentally friendly materials.[4,16–19] In particular, the Eu^{2+}-activated nitride, oxynitride and oxide phosphors, that are variants of the UCr_4C_4 host lattices, have demonstrated significant efficacy

[a] *Max-Planck-Institut für Kohlenforschung, Kaiser-Wilhelm-Platz 1, 45470 Mülheim an der Ruhr, Germany. E-mail: neese@kofo.mpg.de*
[b] *Department of Chemistry, University of Munich (LMU), Butenandtstraße 5-13, 81377 München, Germany*
[c] *Lumileds Phosphor Center Aachen, Lumileds Germany GmbH, Philipsstraße 8, 52068 Aachen, Germany*
[d] *Department of Chemistry, Faculty of Science, Beni-Suef University, Salah Salem Str., 62511 Beni-Suef, Egypt*

† Electronic supplementary information (ESI) available: Tables containing detailed information regarding the different embedded clusters as well as figures containing complementary information regarding the electronic structure, band gap calculations and the computed absorption and emission spectra of the study set of the Eu^{2+}-doped phosphors are provided. See DOI: **https://doi.org/10.1039/d3cp06039j**

in producing a wide variety of narrow-band red and blue-emitting phosphors, characterized by a high degree of tunability and thermal stability.[4,8,16,20–37]

Despite this progress, achieving luminescence tunability in many promising phosphor materials remains a challenging task, especially for narrow band emitting phosphors with rigid structures coupled with limited geometrical flexibility of the activator site, *e.g.*, in solid solution phosphors. In addition, one of the main difficulties lies in the observation of multiple emission signals, which adversely affect their brightness, efficiency, and applicability.[14,32–36,38] This is in particular the case with an increasing number of recently synthesized red emitting phosphors, bearing $Eu^{2,3+}$, Ce^{3+} and Mn^{4+} doping ions in a variety of host structures.[38–40] In this concept, successful applications are mainly based on empirical observations and trial and error implying the urgent need for gaining electronic structure knowledge of these kind of systems.

In general, activated phosphors show systematic geometric and electronic structural properties.[4,21,24,25,41–45] In this framework, we have recently shown the importance of constructing carefully calibrated theoretical spectroscopy protocols.[1] In fact, protocols that are constructed on a systematic basis by combining methods that belong to the density functional theory (DFT) and wavefunction theory (WFT) arsenals have been proven instrumental in defining general descriptors that are able to connect (1) the band gap energy of the Eu^{2+}-doped phosphor and (2) the covalency of the Eu-5d donor orbital involved in the emission process, with the color and the linewidth of the emission band. The availability of such descriptors is of paramount importance as they can be applied as a predictive tool of photoluminescence properties of novel phosphors or to cross-correlate and further validate a large amount of available data that are based on DFT computations,[21,24,25,42,43,46–49] machine learning data analysis[20,50] or empirical correlations[50] towards a systematic design of novel phosphor materials with tailored photoluminescence properties.

To control and optimize the emission properties of Eu^{2+}-doped phosphors, precise management of crystal and ligand field effects within the local environment of the doping center is essential. Various strategies have been proposed, including altering the central metal ions. This approach has demonstrated notable advancements in red-emitting phosphors, such as the transition from the $Ca[LiAl_3N_4]:Eu^{2+}$,[51] (CLA:Eu^{2+}) to $Sr[LiAl_3N_4]:Eu^{2+}$,[23] (SLA:Eu^{2+}) structures in lithoaluminate phosphors. However, it can also introduce drawbacks, as observed with the outlier $Ba[Mg_3SiN_4]Eu^{2+}$,[22] (BMS:Eu^{2+}) compared to $Sr[Mg_3SiN_4]Eu^{2+}$,[26] (SMS:Eu^{2+}) in magnesosilicate phosphors.

Besides the local electronic structure nature of the emissive center, the role of the rigidity of the host environment in terms of its availability for doping, the imposed coordination environment around the doped emissive centers, and the way this influences the phosphor's photoluminescence properties have recently attracted attention. Hence, another versatile approach involves utilizing hosts with multiple doping centers, which offers enhanced diversity and improved control over the structural and electronic properties.[38,52–54] This approach opens new avenues for investigating and optimizing the emission properties of Eu-doped phosphors, ultimately leading to improved performance. In systems with multiple potential doping centers, aspects like the volume of the doping coordination region,[3] the probability of doping and the vibronic coupling of the rigid host structure[55–58] have been successfully employed to interpret the studied phosphor emission properties. In particular, they have been employed to provide insight over the nature of the emission band in room and low temperature spectra of $RbNa[Li_3SiO_4]_2:Eu^{2+}$ [55] and $Sr[LiAl_3N_4]:Eu^{2+}$ [58] or to understand the relationship of the host environment to the heat induced blue shift (HIB) phenomenon in Eu^{2+}-doped phosphors.[59]

With all these considerations in mind, in this work, we aim to present a systematic computational protocol that is strongly intertwined with experimental data and leads our experimental efforts towards the design of novel phosphor materials with desired photoluminescence properties. In particular, we will present the key chemical steps that are required to improve the photoluminescence properties of the well-known $CaBa[LiAl_3N_4]_2:Eu^{2+}$ (CBLA2)[38] red phosphor towards the structural prediction of the yet unknown, $Ca_3Ba[LiAl_3N_4]_4:Eu^{2+}$ (CBLA), Eu^{2+}-doped phosphor that computationally exhibits unprecedented narrow-band red emission properties. For this purpose, we will expand the family of chemical systems that can be treated with the above-described protocol by including a set of phosphors bearing multiple candidate centers for Eu^{2+} doping. Hence besides the known CBLA2 and the target CBLA phosphor, the chosen study set consists of UCr_4C_4-based narrow-band phosphors, namely the alkali lithosilicates $RbNa_3[Li_3SiO_4]_4:Eu^{2+}$ (RNLSO)[52] and $RbNa[Li_3SiO_4]_2:Eu^{2+}$ (RNLSO2)[53] as well as, the isotypical to RNLSO2, nitridolithoaluminate $CaBa[LiAl_3N_4]_2:Eu^{2+}$ (CBLA2).[38] It is demonstrated that the electronic structure of the known CBLA2, RNLSO, and RNLSO2 is understood, and the isotypic to RNLSO, CBLA Eu^{2+}-doped phosphor fulfils the requirements for narrow band red emission.

II. Study set of phosphors and geometrical properties

Three well known Eu^{2+}-doped UCr_4C_4-based phosphors are selected for the study set on the basis of the following criteria: (1) they emit in the wide range between the infrared, red, cyan and blue range of the optical spectrum, (2) they contain multiple candidate doping centers that are available for the Eu^{2+} activator ion in a variation of coordination environments and (3) they show a variation of emission signals containing a single band or multiple bands occurring at various energies and intensities. In particular, the study set consists of the red and near-infrared emitting Eu^{2+}-doped nitridolithoaluminate phosphor $CaBa[LiAl_3N_4]_2:Eu^{2+}$, abbreviated as (CBLA2:$Eu^{2+}$)[38] and is completed by the blue and cyan emitting Eu^{2+}-doped alkali lithosilicate phosphors $RbNa_3[Li_3SiO_4]_4:Eu^{2+}$ (RNLSO:Eu^{2+})[52] and $RbNa[Li_3SiO_4]_2:Eu^{2+}$ (RNLSO2:Eu^{2+}).[53] The atomic arrangements are visualized in Fig. 1. RNLSO adopts the tetragonal ($I4/m$)

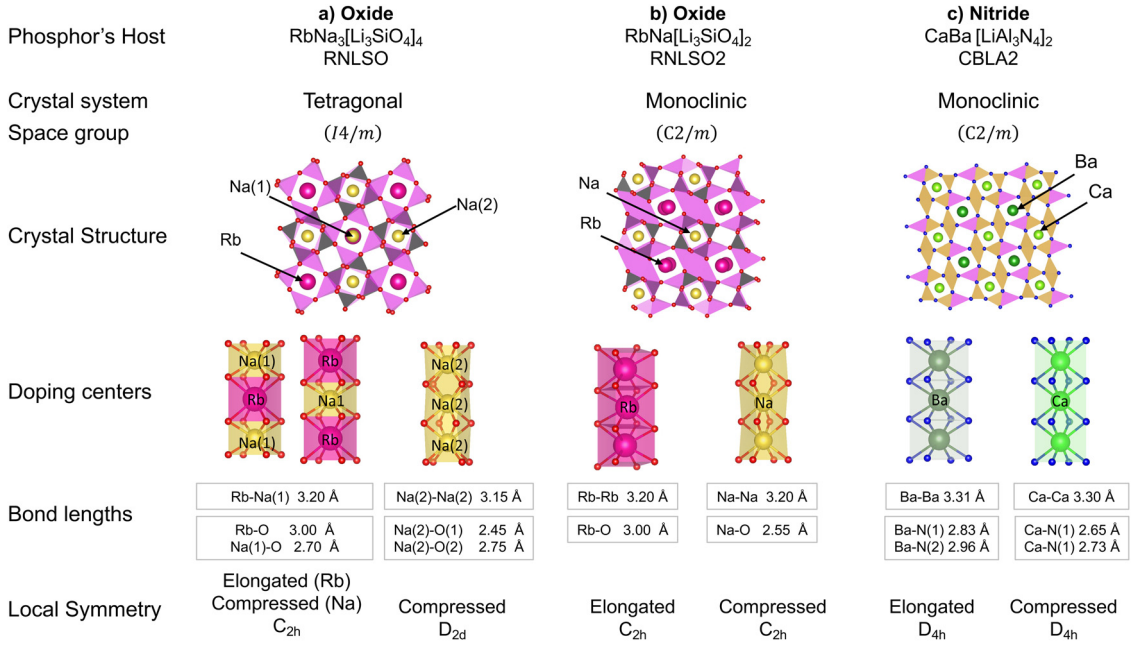

Fig. 1 The crystal structure and space group of the studied phosphors' hosts: RNLSO, RNLSO2, and CBLA2. The probable cationic doping site for each structure, together with the most important bond lengths, and symmetry labels around the probable sites are also provided. Atom colors: Rb (dark red), Na (yellow), Ca (light green), Ba (deep green), Si (dark gray), Al (yellowish pink), Li (pink), N (blue), and O (red).

space group while CBLA2 and RNLSO2 crystallize in the monoclinic ($C2/m$) space group. All host crystal structures adopt a rigid UCr_4C_4 structure type with highly condensed tetrahedra networks built by vertex- and edge-sharing tetrahedra. Namely, $(Al/Li)N_4$ nitride tetrahedra in CBLA2 and $(Si/Li)O_4$ oxide tetrahedra in both RNLSO and RNLSO2. The tetrahedral network forms *vierer*-ring channels, which could be empty or filled with cations ((Ca^{2+}/Ba^{2+}) or (Na^{+}/Rb^{+})). These cations form nitride $(Ca^{2+}/Ba^{2+})N_8$ or oxide $(Na^{+}/Rb^{+})O_8$ cuboids, respectively. In RNLSO2 and CBLA2, the occupied channel has only one type of cation, hence along the principle symmetry rotation axis, cuboid sequences are formed with $(Rb^{+}–Rb^{+}–Rb^{+}$, $Na^{+}–Na^{+}–Na^{+})$ and $(Ba^{2+}–Ba^{2+}–Ba^{2+}$ and $Ca^{2+}–Ca^{2+}–Ca^{2+})$ central cation building units, respectively. In contrast, in the case of RNLSO, $Na(1)^{+}$ and Rb^{+} are alternating in the same channel forming cuboid sequences with $Na(1)^{+}–Rb^{+}–Na(1)^{+}$ (or equivalently $Rb^{+}–Na(1)^{+}–Rb^{+}$) central cation building units as well as $Na(2)^{+}–Na(2)^{+}–Na(2)^{+}$ ones. In CBLA2, two different double chains can be distinguished, one composed solely of AlN_4 tetrahedra and one composed of one single chain of AlN_4 tetrahedra and one single chain of LiN_4 tetrahedra.

In Fig. 1, the probable cation sites for Eu^{2+} doping are highlighted. The selection of the doping sites is based on (1) the similarity of their ionic radii (r) to Eu^{2+} [60] and (2) their suitability for Eu^{2+} doping in a host environment that minimizes the steric effects.[3] In fact, as seen in Table 1, Eu^{2+} doping with Ca^{2+} and Na^{+} is expected to form strained EuL_8 (L is N^{3-}/O^{2-}) cuboids with $r_{Ca^{2+}–Eu^{2+}} = -0.19$ Å and $r_{Na^{+}–Eu^{2+}} = -0.07$ Å and EuL_8 cuboid volume that varies between 29.5 Å^3 and 30.1 Å^3. In contrast, Eu^{2+} doping at Ba^{2+} and Rb^{+} is expected to form rather relaxed EuL_8 cuboids with $r_{Ba^{2+}–Eu^{2+}} = 0.10$ Å and

Table 1 Structural and geometrical information of cuboid ML_8, (L = N or O) at the different candidate doping centers for CBLA2 (M = Ba^{2+} or Ca^{2+}), RNLSO (M = Rb^{+}, $Na(1)^{+}$ or $Na(2)^{+}$) and RNLSO2 (M = Rb^{+} or Na^{+}) in terms of M ionic radii, M–L bond distances and the first coordination shell cationic compositions. $\Delta r_{M^{m+}–Eu^{2+}}$ is the difference in the ionic radii between the replaced ion (M^{m+}, m = 1, 2) and Eu^{2+}, at cuboid 8-fold coordination, where the ionic radius of Eu^{2+} = 1.25 Å. The DFT(PBE0) ligand field splitting (ΔE_{LF}) of the Eu 5d orbital and the energy separation between barycenters of 4f–5d manifolds (ΔE_{fd}) are also provided

Phosphor	Doping site (M^{m+})	Ionic radii (r) (Å)[60]	$\Delta r_{M^{m+}–Eu^{2+}}$ (Å)	Average M–L bond distance (Å)	Volume of ML_8 cuboid (Å^3)	First shell cations	ΔE_{fd} (eV)	ΔE_{LF} (eV)
$CaBa[LiAl_3N_4]_2$:Eu^{2+} CBLA2	Ba^{2+}	1.35	0.10	2.90	37.60	$[Li_4Al_4]^{16+}$	3.08	2.17
	Ca^{2+}	1.06	−0.19	2.70	29.50	$[Al_8]^{24+}$	1.06	4.63
$RbNa_3[Li_3SiO_4]_4$:Eu^{2+} RNLSO	Rb^{+}	1.61	0.36	3.00	40.00	$[Li_8]^{8+}$	4.16	1.60
	$Na(1)^{+}$	1.18	−0.07	2.70	30.17	$[Li_8]^{8+}$	2.94	3.06
	$Na(2)^{+}$	1.18	−0.07	2.60	30.61	$[Li_4Si_4]^{20+}$	2.42	3.60
$RbNa[Li_3SiO_4]_2$:Eu^{2+} RNLSO2	Rb^{+}	1.61	0.36	3.00	40.50	$[Li_4Si_4]^{20+}$	3.03	2.02
	Na^{+}	1.18	−0.07	2.60	29.45	$[Li_8]^{8+}$	2.38	3.68

$r_{Rb^+–Eu^{2+}}$ = 0.36 Å and EuL_8 cuboid volume that varies between 37.6 Å^3 and 40.5 Å^3. In particular, the Eu^{2+}-doped CBLA2 phosphor has two candidate doping centers at Ca^{2+} and Ba^{2+} positions. RNLSO phosphor has three candidate doping centers at $Na(1)^+$, $Na(2)^+$ and Rb^+ positions. Finally, RNLSO2 phosphor has two candidate doping centers at Na^+ and Rb^+ positions.

As shown in Fig. 1, CBLA2 is isotypic to RNLSO2, hence Eu^{2+} doping at Ca^{2+} and Ba^{2+} centers form compressed and elongated EuN_8 cuboids of C_{2h} symmetry with average bonding or interatomic distances of (Ca/Eu)–N 2.65–2.75 Å and (Eu/Ca)–Ca 3.30 Å while (Eu/Ba)–N 2.83–2.96 Å and (Eu/Ba)–Ba is 3.31 Å. These cuboids deviatefrom the 'ideal' D_{4h} symmetry by only 1–2%. In the case of RNLSO, Eu^{2+} doping at $Na(1)^+$ or Rb^+ centers forms compressed and elongated EuO_8 cuboids with C_{2h} symmetry, respectively, with an average bond distance of (Na(1)/Eu)–O ∼ 2.71 Å and (Rb/Eu)–O ∼ 3.01 Å. In contrast, Eu^{2+} doping at $Na(2)^+$ centers forms compressed cuboids with D_{2d} symmetry with (Na(2)/Eu)–O 2.45–2.75 Å. Similarly, in the case of RNLSO2 Eu^{2+} doping at $Na(1)^+$ or Rb^+ centers form compressed and elongated EuO_8 cuboids of C_{2h} symmetry, respectively, with an average bond distance of (Na/Eu)–O 2.55 Å and (Rb/Eu)–O 3.00 Å.

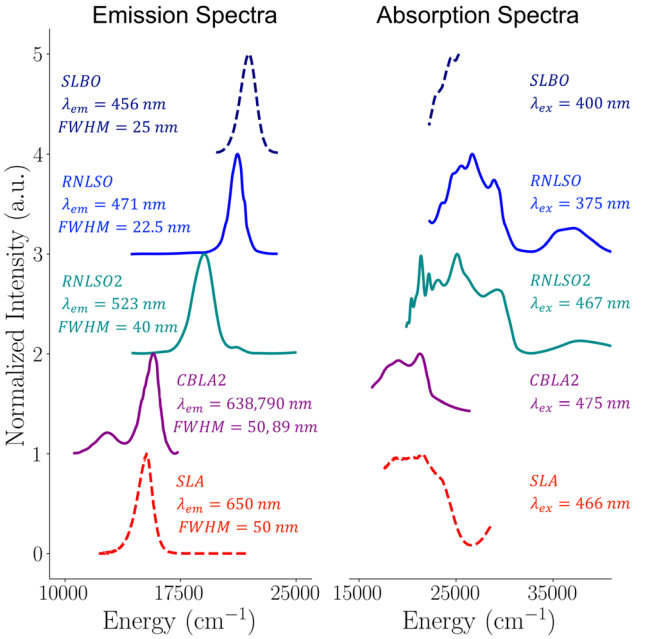

Fig. 2 Experimental emission (left) and absorption (right) spectra of Eu^{2+}-doped phosphors with multiple doping centers (RNLSO in solid blue, RNLSO2 in solid dark-cyan and CBLA2 in solid dark-magenta) compared with previously studied phosphors (SLA in dotted red, and SLBO in dotted navy-blue).

III. Experimental spectra

The experimental absorption and emission spectra of the nitride (CBLA2:Eu^{2+})[38] and oxide (RNLSO:Eu^{2+} and RNLSO2:Eu^{2+})[52,53] phosphors are shown in Fig. 2. The absorption spectra show broad bands and shift towards higher energies in the sequence CBLA2 (15 000–25 000 cm^{-1}) to RNLSO2 (22 000–40 000 cm^{-1}) and RNLSO (24 000–40 000 cm^{-1}). Upon applying a laser excitation, all studied cases show a main emission narrow band that shifts also towards higher energies in the same sequence.

In particular, CBLA2:Eu^{2+}, upon excitation with a 444 nm laser, exhibits an intense, narrow red emission band at 639–636 nm (15 650–15 723 cm^{-1}) with FWHM 48–57 nm (∼1095–1266 cm^{-1}) and a weak broad infrared (IR) emission band at 790 nm (12 660 cm^{-1}) and FWHM ∼89 nm (∼1430 cm^{-1}). The intensity of the later band improves with increasing Eu^{2+} doping concentration. The two bands have been assigned to emission from Eu^{2+}-doped centers at Ba^{2+} and Ca^{2+} positions, respectively.[38] In contrast, RNLSO:Eu^{2+} upon excitation with a 400 nm laser exhibits a single narrow blue emission band at 471 nm (21 230 cm^{-1}) with a FWHM of 22.5 nm (∼1015 cm^{-1}).[52] In the case of RNLSO2, two bands show up when a variety of excitation lasers in the 400 nm region is employed.[53] A high intensity narrow green emission band appears at 523 nm (19 120 cm^{-1}) with a FWHM of 40 nm (∼1465 cm^{-1}). A second weaker intensity cyan emission band occurs at higher energies (472 nm, 21 185 cm^{-1}). These bands have been ascribed to Eu^{2+}-doped centers at Na^+ and Rb^+ positions, respectively, while it has been shown that their relative intensity varies with the Eu^{2+} doping concentration at the Na^+ and Rb^+ positions.[52,55]

As seen in Fig. 2, the study set of phosphors lies between the absorption and emission characteristics of two well-known narrow band phosphors, namely the red emitting nitride SLA:Eu^{2+}[23] and the blue emitting oxide SLBO:Eu^{2+}[16] phosphors. While SLBO:Eu^{2+} contains a single doping site for Eu doping, in SLA:Eu^{2+}, there are in principle two doping candidate sites. The two sites have a similar local geometric structure, but they are not identical. Hence while at room temperature within the experimental resolution, the two sites provide similar absorption spectra and emission spectra,[1] it has been recently shown that at low temperature, they provide unique emission band signatures in the vibrationally resolved emission spectrum.[58] These phosphors define the lower and upper boundaries of a range of Eu^{2+} doped phosphors in which the crystal field strength as well as the Eu/ML_8 cuboid compression is increasing.[1] It should be noted that the actual bottom boundary in the Eu^{2+}-doped phosphors is defined by the narrow band red emitting $Ca[LiAl_3N_4]$:Eu^{2+} (CLA:Eu^{2+}) phosphor.[51] As seen, the CBLA2:Eu^{2+} emission spectrum is blue shifted by +300 cm^{-1} with respect to the SLA:Eu^{2+} one, showing a similar bandwidth range, FWHM ∼ 50 nm (1090 cm^{-1}). Likewise, the RNLSO:Eu^{2+} emission spectrum is red shifted by 700 cm^{-1} with respect to the SLBO:Eu^{2+} one, showing again a similar bandwidth range in the ultranarrow band regime, FWHM ∼ 22–25 nm (1010–1220 cm^{-1}). RNLSO2 lies in between the above described cases indicating that complex phosphors with multiple candidate doping centers might still show linear property characteristics like the single doping center phosphors.

To conclude this part, while RNLSO:Eu^{2+} show a unique blue emission band. RNLSO2:Eu^{2+} shows a predominant cyan emission band and a blue emission band with higher energy and weaker intensity, where the relative intensity of the bands is

tunable by the chosen excitation wavelength (Fig. S9 and S10, ESI†). The isotypic to RNLSO2:Eu^{2+} and CBLA2:Eu^{2+} shows a broad IR band besides the main red emission band. In principle, the presence of a second or multiple bands besides the main emission band is undesirable in the novel phosphor design efforts as they may reduce effectively their brightness, performance and efficiency. While in the case of RNLSO2:Eu^{2+}, the higher energy, second weaker intensity blue emission band is tunable by the choice of the laser excitation energy,[53] the IR band in CBLA2:Eu^{2+} can only be suppressed at low Eu^{2+} doping concentrations.[38] This emphasizes the urgent need for advancing the information content of the emission intensity mechanism in these materials.

IV. Computational strategy

1. Computational details

All calculations were performed employing the ORCA 5.0 suite of programs.[61–64] Crystal structures' coordinates were taken from the crystallographic data,[38,52,53] refined based on the experimental crystallographic X-ray diffraction. All clusters were constructed on the basis of the embedded cluster approach. In all calculations, the def2-TZVP basis set of the Ahlrichs group[65,66] was used for all main group element atoms while for Eu, the segmented all-electron relativistically re-contracted (SARC) scheme[67–70] was employed. The calculations were accelerated by employing the resolution of identity approximation (RI)[71] for the Coulomb integrals, while the exchange terms were efficiently computed using the 'chain-of-spheres' (COSX)[72,73] approximation by utilizing the SARC/J coulomb fitting and def2-TZVP/C correlation auxiliary basis sets, respectively. Second-order Douglas–Kroll–Hess relativistic corrections (DKH2)[74,75] were used throughout to account for scalar relativistic effects, employing the finite nucleus model.[76] The Hartree–Fock (HF) layers used in the embedding cluster calculations were equipped with a minimal LANL2DZ basis set with the respective HayWadt ECPs.[77–80]

The optical band gap of the host structures was calculated by the similarity transformed equation of motion domain-based local pair natural orbital coupled cluster singles and doubles (STEOM-DLPNO-CCSD)[81,82] as well as TD-DFT[83] methods. In the latter, a collection of DFT functionals were chosen, belonging to the GGA:PBE,[84] hybrid:PBE0,[85–87] range separated hybrid: CAM-B3LYP,[88] double hybrid: B2PLYP,[89] and range separated double hybrid: ωB2PLYP[90] families. Similarly, TD-DFT and complete active space (SA-CASSCF)[91,92] methods in conjunction with the second order N-electron valence state perturbation theory (NEVPT2)[93,94] including spin–orbit coupling (SOC) were employed to compute the band gap energies of the Eu^{2+}-doped structures. As briefly discussed in the computational considerations Section IV.3 and in detail in section SII of the ESI,† based on these results, the TD-DFT/PBE0 was chosen for the production calculations. Preliminary calculations for estimating the multi-root nature of the Eu^{2+}-doped phosphor emission process and the effect of SOC and spin state energetics of the emission bands were performed employing SA-CASSCF(7,19)/NEVPT2/SOC. As discussed in section IV.3, the SOC interactions do not significantly influence the emission band energy positions, hence they were excluded from the production calculations. Eu^{2+} doping energies at different candidate sites were computed at DFT/PBE0 and DLPNO-CCSD(T) levels of theory.[95–97] DLPNO-CCSD(T) doping energies were decomposed into chemically meaningful energies on the basis of local energy decomposition (LED) approach[98,99] starting from quasi-restricted (QRO)[100] Kohn Sham (KS) orbitals.

At different Eu^{2+} doping sites, absorption spectra were computed at TD-DFT/PBE0 employing the Tamm–Dancoff approximation (TDA)[101] accompanied by the Natural Transition Orbital (NTO) analysis for the computed bands. Photoluminescence spectra were computed using TD-DFT/TDA/PBE0 employing the excited state dynamics (ESD) path integral protocol[102–104] in which vibronic coupling is included within the Frank–Condon and Herzberg–Teller coupling schemes. In this framework, the ground state Hessian was calculated at the DFT/PBE0 level while the excited state geometry and Hessian obtained by approximating excited state PES through the vertical gradient (VGFC) model as discussed in the ESD module.[104]

A constant Gaussian broadening was used for all presented absorption and emission spectra which amounts to an FWHM of 1500 cm^{-1} and 500 cm^{-1}, respectively. For better visual agreement with the experimental absorption spectra, a second Gaussian broadening with an FWHM of 3000 cm^{-1} was used in some of the computed absorption spectra.

2. Construction of the cluster models

All cluster models were constructed on the basis of the embedded cluster approach.[105–108] In the chosen scenario, the embedded cluster model consists of four regions (Fig. 3): the quantum cluster (QC), a region that is used to neutralize the charged QC cluster, referred to also as a Hartree–Fock region (HF) in the multiscale approaches,[109] the boundary region (BR, also called an ECP region), and the point charge (PC) region. All regions are extracted from the respective crystallographic supercells. Further information about the employed cluster models is provided in Section SI of the ESI,† Fig. S1 and Table S1.

As shown in Fig. S1 (ESI†), the series of the chosen cluster models consists of sequences of cuboidal structures ranging from monomers to pentamers. The low doping limit is considered so that Eu^{2+}-doped structures contain only one Eu^{2+} ion replacing one (Ca^{2+}, Ba^{2+}, Na^{+}, or Rb^{+}) cation per cluster.[60] In addition, no (Eu^{2+}–Eu^{2+}) interaction is expected, as well, no other cation substitution (*e.g.*, Li^{+}, Mg^{2+}, Al^{3+}, or Si^{4+}) or occupation of interstitial sites is expected due to structural and steric reasons.[1] Owing to the strong rigidity of the considered solid-state crystal structures, no further structural relaxation due to Eu^{2+} doping needs to be taken into account.

3. Computational considerations

As discussed in detail in Sections SII and SIII of the ESI† (cluster size convergence – choice of the computational protocol, computational protocol summary), the cluster size convergence was evaluated on the basis of the band gap energies of the host structures and the entire absorption spectra of the

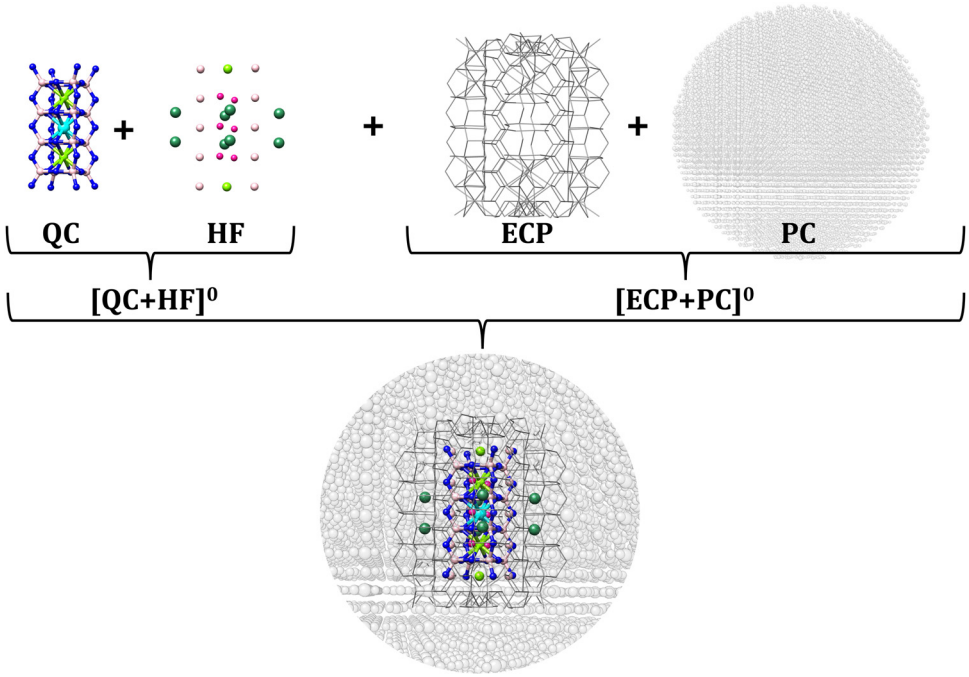

Fig. 3 Schematic representation of the embedded cluster approached employed, shown for the trimer cluster of CBLA2:Eu^{2+}-doped in the Ca^{2+} center, as well an embedding scenario applied to achieve charge neutrality of the clusters. Gray lines and spheres represent the cECPs and point charges in the BR and PC regions, respectively. For QC and HF regions, the atom colors are as follows; Eu (cyan), Ca (light green), Ba (deep green), Al (yellowish pink), Li (pink), and N (blue).

Eu^{2+} doped structures. For this purpose, the band gap energies and excitation spectra were computed employing wavefunction based levels of theory STEOM-DLPNO-CCSD and SA-CASSCF/NEVPT2, respectively, as well as various TD-DFT levels of theory. Based on this analysis, trimer structures are chosen for the production calculations and analysis of the absorption and emission processes employing the TD-DFT/PBE0 computational protocol in conjunction with the excited state dynamics (ESD).

V. Results and discussion

1. Predicting the most probable site for Eu^{2+} doping (doping descriptor)

Prior entering the spectra computation and analysis sections, the major question that arises is how probable Eu^{2+} doping is each of the Ca^{2+}, Ba^{2+}, Na^{+}/$Na(1)^{+}$/$Na(2)^{+}$ and Rb^{+} host positions in the study set of CBLA2 as well as RNSLO and RNSLO2 phosphors. DLPNO-CCSD(T) levels of theory were employed to address this question.

It should be noted that in RNLSO and RNLSO2, charge compensation for singly charged ion replacements (Na/Rb) is achieved through charge redistribution within the employed embedded cluster scheme. This allows for the electronic relaxation around the Eu^{2+} doped centers in terms of electrostatic and covalent Eu-host interactions. Details regarding the principles of this analysis are provided in Section SIII.1-2 of the ESI.† Focusing on CBLA2 as shown in Table 2 and Fig. 4, DLPNO-CCSD(T) results predict that Eu^{2+} doping at Ba^{2+} centers provides more stable structures with respect to Eu^{2+} doping at Ca^{2+} centers by 3 eV. Similarly, in RNLSO2 Eu^{2+}, the doping at Rb^{+} centers provides more stable structures with respect to Eu^{2+} doping at Na^{+} centers by $\sim$2.5 eV. In contrast, in RNLSO, Eu^{2+} doping at (Rb^{+}, $Na(1)^{+}$) centers provides close DLPNO-CCSD(T) doping energies (−1.66, −1.32 eV) while Eu^{2+} doping at $Na(2)^{+}$ provides rather less stable structures (−0.88 eV).

Table 2 Eu^{2+} doping energies (eV) for RNLSO, RNLSO2 and CBLA2 at the different candidate doping centers of trimer clusters computed using DLPNO-CCSD(T) methods

Phosphor	Doping site	Doping energy (eV)
CBLA2	Ba^{2+}	−3.67
	Ca^{2+}	−0.67
RNLSO	$Na(1)^{+}$	−1.32
	$Na(2)^{+}$	−0.88
	Rb^{+}	−1.66
RNLSO2	Na^{+}	−0.87
	Rb^{+}	−3.34

DLPNO-CCSD(T) results are used as a basis for the quantitative analysis of the doping energy in terms of ionic and covalent interactions as they collectively describe the various interactions in the framework of the local energy decomposition (LED) analysis as presented for CBLA2:Eu^{2+} in Fig. 4 and in Section III.2 of the ESI.† As has been shown in several studies[110,111] local energy decomposition (LED) enables the classification of interactions into different types of meaningful chemical and physical interactions, thereby facilitating a comprehensive exploration of the electronic structure and the ionic and covalent interactions surrounding the Eu ions in their respective environments.

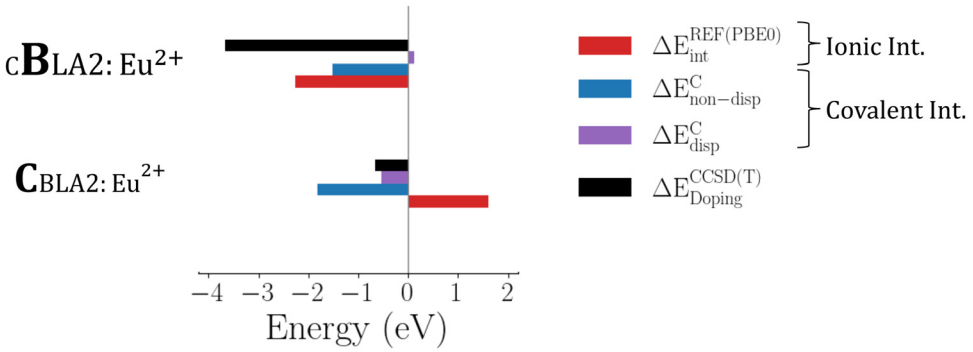

Fig. 4 Local energy decomposition (LED) analysis of DLPNO-CCSD(T) doping energies (black bars) for CBLA2:Eu^{2+} at the probable sites for Eu^{2+} doping (Ca^{2+}, or Ba^{2+}) in terms of ionic (E_{int}^{REF}) and covalent ($E_{non\text{-}disp}^{C}$, E_{disp}^{C}) interactions, shown in red, blue, and purple bars, respectively.

As shown in Fig. 4 and Fig. S7 (ESI†), the least probable site for each system (CBLA:Eu^{2+} at Ca^{2+}, RNLSO2:Eu^{2+} at Na^{+}, and RNLSO:Eu^{2+} at $Na(2)^{+}$, respectively) shows positive ionic interactions as they are expressed by E_{int}^{REF} = +1.8, +0.9 and +1.1 eV, respectively, indicating the unavailability of the host structure for Eu^{2+} doping due to the significant compression in the EuL_8 cuboid. This is also accompanied by the shorter Eu–L ligand and strong repulsion with the first shell of cations, as shown in Table 1. In contrast, the most probable site for each system exhibits strong and negative electrostatic interactions ($\sim E_{int}^{REF}$ = −2.3, −3.0 and −1.4 eV) for CBLA2:Eu^{2+} at Ba^{2+}, RNLSO2:Eu^{2+} at Rb^{+}, and RNLSO:Eu^{2+} at Rb^{+}, respectively.

The relevant covalent type interactions ($E_{non\text{-}disp}^{C}$, E_{disp}^{C}) result in rather fine tuning of the doping energy. In particular, dispersion corrections follow the difference in the ionic radii between the substituted cations and Eu^{2+} (Table 1). They are hence repulsive in the most probable and more relaxed EuL_8 cuboids of CBLA2:Eu^{2+} at Ba^{2+}, RNLSO2:Eu^{2+} at Rb^{+}, and RNLSO:Eu^{2+} at Rb^{+}, respectively. Similarly, as expected, stronger non-dispersion corrections are observed in the more covalent nitride (CBLA2) with respect to the oxide (RNLSO and RNLSO2) phosphors. Compressed *versus* elongated EuL_8 cuboids show also larger non-dispersion interactions that are associated with stronger Eu–N/O covalent interactions and bond lengths according to Table 1. Finally, the most stable EuL_8 cuboids also show the smallest triple corrections across the study set that are inverted proportional to the doping energy.

The above quantitative analysis demonstrates the direct connection of the cuboid characteristics of a given host ion with its probability for Eu^{2+} doping. This indicates that relaxed host cuboids have in general a higher tendency for Eu^{2+} doping.

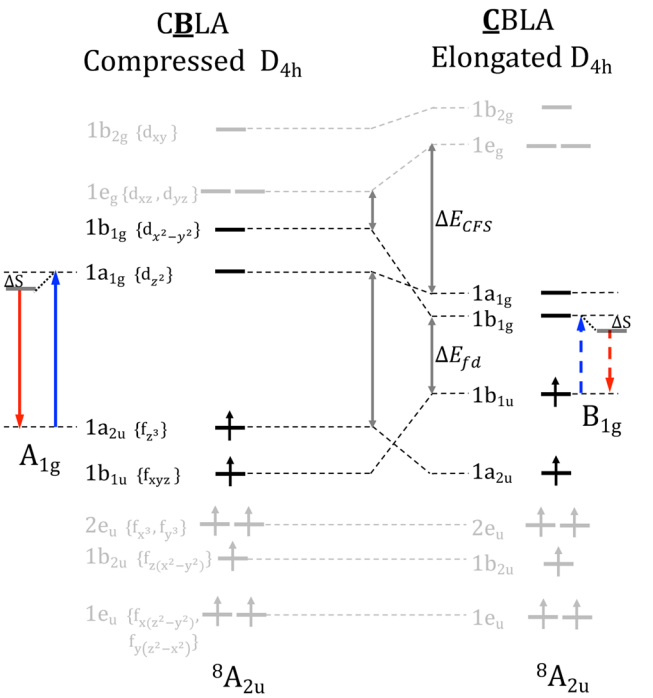

Fig. 5 Molecular orbital diagram of the CBLA2:Eu^{2+} phosphor at the two Eu^{2+}-doped centers, Ca^{2+} (left) and Ba^{2+} (right), where they adopt compressed and elongated D_{4h} [EuN_8] cuboids, respectively. The involved electronic transitions consisting of the absorption and emission processes are adopted with the 1-electron picture. Blue and red arrows indicate the most important absorption and relevant emission processes, respectively. Dotted arrows indicate dipole forbidden transitions. ΔE_{LF}, ΔE_{fd} and ΔE_S, represent the ligand field splitting of Eu 5d, the energy separation between barycenters of Eu 4f–5d manifolds, and the expected Stokes shift, respectively.

VI. Designing a CBLA:Eu^{2+}-doped phosphor with potentially improved emission properties

1. Insights into the emission intensity mechanism of CBLA2:Eu^{2+} phosphor

Eu^{2+} doping in the Ba^{2+} center forms tetragonally elongated (D_{4h}) EuN_8 cuboids. This leads to absorption and emission processes consisting of the *z*-polarized dipole allowing Eu $4f_{z^3} \leftrightarrow$ Eu $5d_{z^3}$ electron transitions and decays (Fig. 5). In contrast, doping at the Ca^{2+} center leads to a strongly tetragonally compressed (D_{4h}) EuN_8 cuboid. As shown in Table 1, in comparison to the tetragonally elongated cuboids, the ligand field splitting of Eu 5d-shell, ΔE_{LF} is increased while the energy separation between barycenters of Eu 4f–5d manifolds, ΔE_{fd}, is decreased rather strongly leading to red-shifted absorption and emission processes consisting of the dipole forbidden Eu $4f_{xyz} \leftrightarrow$ Eu $5d_{x^2-y^2}$ electron transitions and decays (Fig. 5). This is in accordance with the fact that the color of the phosphors is associated with the predominant Eu-4f $\leftrightarrow$ Eu-5d transition.[1]

Entering the spectra computation section, as shown in Fig. 6, in the case of CBLA2, the main emission band arises from absorption band 2. The emission process involves a Eu^{2+} center doped at the Ba^{2+} site and takes place from a Eu $5d_{z^2}$ based molecular orbital MO with a covalency factor a^2 = 0.94. In contrast, the lower energy and weak intensity emission band arise from absorption band 1. The emission process involves a Eu^{2+} center doped at the Ca^{2+} site involving a Eu $5d_{x^2-y^2}$ based molecular orbital MO with a covalency factor a^2 = 0.87. Absorption band 3 arises from a Eu^{2+} center doped at the Ca^{2+} site and involves a Eu $4f_{y(3x^2-y^2)} \rightarrow$ Eu $5d_{x^2-y^2}$ electron excitation showing no pronounced emission intensity. Likewise, the high energy absorption band 4 arises from a Eu^{2+} center doped at the Ba^{2+} site and involves an Eu $4f_{xyz} \rightarrow$ Eu $5d_{x^2-y^2}$ electron excitation showing a negligible emission intensity.

It should be noted that symmetry reduction towards C_{2h} or S_4 symmetric EuN_8 cuboids could render the Eu $4f_{xyz} \leftrightarrow$ Eu $5d_{x^2-y^2}$ electron decay a dipole allowed process. As shown in Fig. S8 (ESI†) this is in fact the case for both the isotypic to CBLA2, RNLSO2 but also RNLSO rendering in particular the Eu^{2+} doping at Na and Na(1) centers, respectively, a dipole allowed Eu $4f_{xyz} \leftrightarrow$ Eu $5d_{x^2-y^2}$ emissive process. As discussed in detail in Section SIII.3 of the ESI,† these positions dominate the experimental spectra. In fact, in contrast to CBLA2 in the case of RNLSO2 (Fig. S9a, ESI†), the main emission band 1* arises from Eu^{2+} centers doped at the Na^+ sites (in relation to Ca^{2+} sites in CBLA2) and takes place from the non-bonding Eu $5d_{x^2-\ y^2}$ based MO with a^2 of 0.92. A weak blue shifted emission band 2* arises from Eu^{2+} centers doped at the Rb^+ sites (in relation to Ba^{2+} sites in CBLA2) reached by absorption band 2 and takes place from the non-bonding Eu $5d_{z^2}$ based MO with a^2 = 0.97. As shown in Fig. S10 (ESI†) and according to the experiment, the intensity of this second band can be tuned by the excitation laser. In the case of RNLSO (Fig. S9b, ESI†), the main emission band arises from a Eu^{2+} center doped at the $Na(1)^+$ site and takes place again from the non-bonding Eu $5d_{x^2-y^2}$ based MO with a^2 of 0.95.

It should be emphasized that the emission bands arising from Eu^{2+} centers doped at Ca^{2+}, Na^+ and $Na(1)^+$ sites in the case of CBLA2, RNLSO2 and RNLSO have the following characteristics (1) involve compressed EuN_8 and EuO_8 cuboids, (2) take place from non-bonding Eu $5d_{x^2-y^2}$ based MO and (3) the RNLSO band is blue shifted (FWHM = 1015 cm^{-1}, 22.5 nm) with respect to the RNLSO2 (FWHM = 1465 cm^{-1}, 40 nm) band by 2100 cm^{-1} with a narrower bandwidth by 450 cm^{-1}, respectively. Hence, there is a clear relation between the geometric characteristics around the Eu^{2+} centers and their emission properties in these systems. This is consistent with the descriptor relationships discussed in Section S IV, Fig. S11, and Table S5 (ESI†).

Up to this point of analysis, it has been shown that owing to the very rigid nature of the emissive states in both Eu^{2+}-doped phosphors bearing one or multiple doping centers, the TDDFT/PBE0 computed spectra provide satisfactory agreement to the experimentally observed absorption and emission spectral features allowing for a quantitative analysis. However, for the identification of the probable Eu^{2+}-doping centers at the ground state and a comprehensive qualitative and quantitative description that connects the strength of electrostatic and covalent interactions between Eu^{2+} and the coordination environment provided by the phosphor host structure, the sensitivity provided by DLPNO-CCSD(T) computed energies and their respective LED analysis is required. These two successful approaches will be employed below towards an *in silico* investigation of new Eu^{2+} doped phosphor with tailored photoluminescence properties.

2. The impact of the host environment on the emission properties of the Eu^{2+}-doped phosphors

In the next step, we investigate the effect of the host environments on the electronic structure, chemical bonding and consequently emission properties of the studied phosphors.

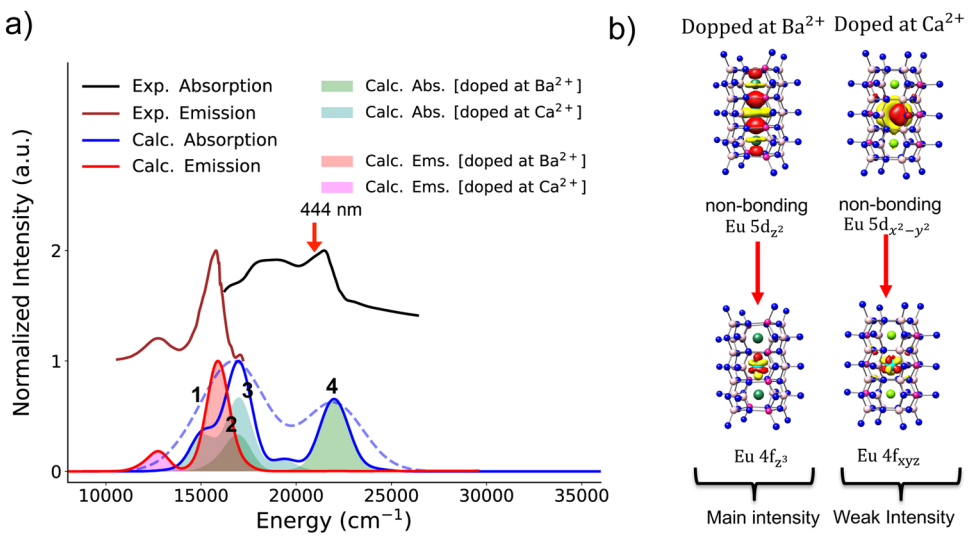

Fig. 6 (a) Experimental (black), calculated TDDFT/PBE0 absorption (blue; solid and dashed lines plotted with Gaussian broadening 1500, 3000 cm^{-1}, respectively) spectra and experimental (brown), ESD/TDDFT/PBE0 calculated (red) emission spectra. Filled colored bands indicate individual contributions of the different Eu^{2+}-doped centers. (b) 1st transition responsible for emission upon relaxation for all the candidate Eu^{2+}-doped centers. The red arrow indicates the laser energy in the emission experiment.

The results are summarized in Fig. 7, emphasizing the structural transformation from RNLSO2 to RNLSO, highlighting its profound impact on electronic structure and bonding, resulting in a significant enhancement in emission properties. It can be applied similarly to enhance CBLA2, toward CBLA thereby advancing its properties.

As shown in Fig. 7a, in the case of RNLSO, the $Na(1)^+$ sites form host cuboids ($Na(1)^+O_8$) that are tetragonally compressed with respect to the (Na^+O_8) cuboids in RNLSO2, owing to the formation of the Rb^+–$Na(1)^+$–Rb^+ cuboid sequence. As discussed in the previous sections, these sites dominate the emission bands in the respective Eu^{2+}-doped phosphors. In particular, $Na(1)^+$ centers have a higher probability for Eu^{2+}-doping with respect to the Na^+ sites in RNLSO2 while they result in emission bands that are blue shifted and narrower. The local energy decomposition (LED) analysis confirms that Eu^{2+} doping at the Na^+ sites in RNLSO2 results in repulsive ionic interactions with the $[O_8Li_4Si_4Na_2]^{6+}$ host environment that is only partially compensated by attractive covalent interactions leading to an overall low probability for Eu^{2+} doping in these centers. In contrast, Eu^{2+} doping at the Rb^+–$Na(1)^+$–Rb^+ tetragonally compressed cuboid sequence in RNLSO shows almost

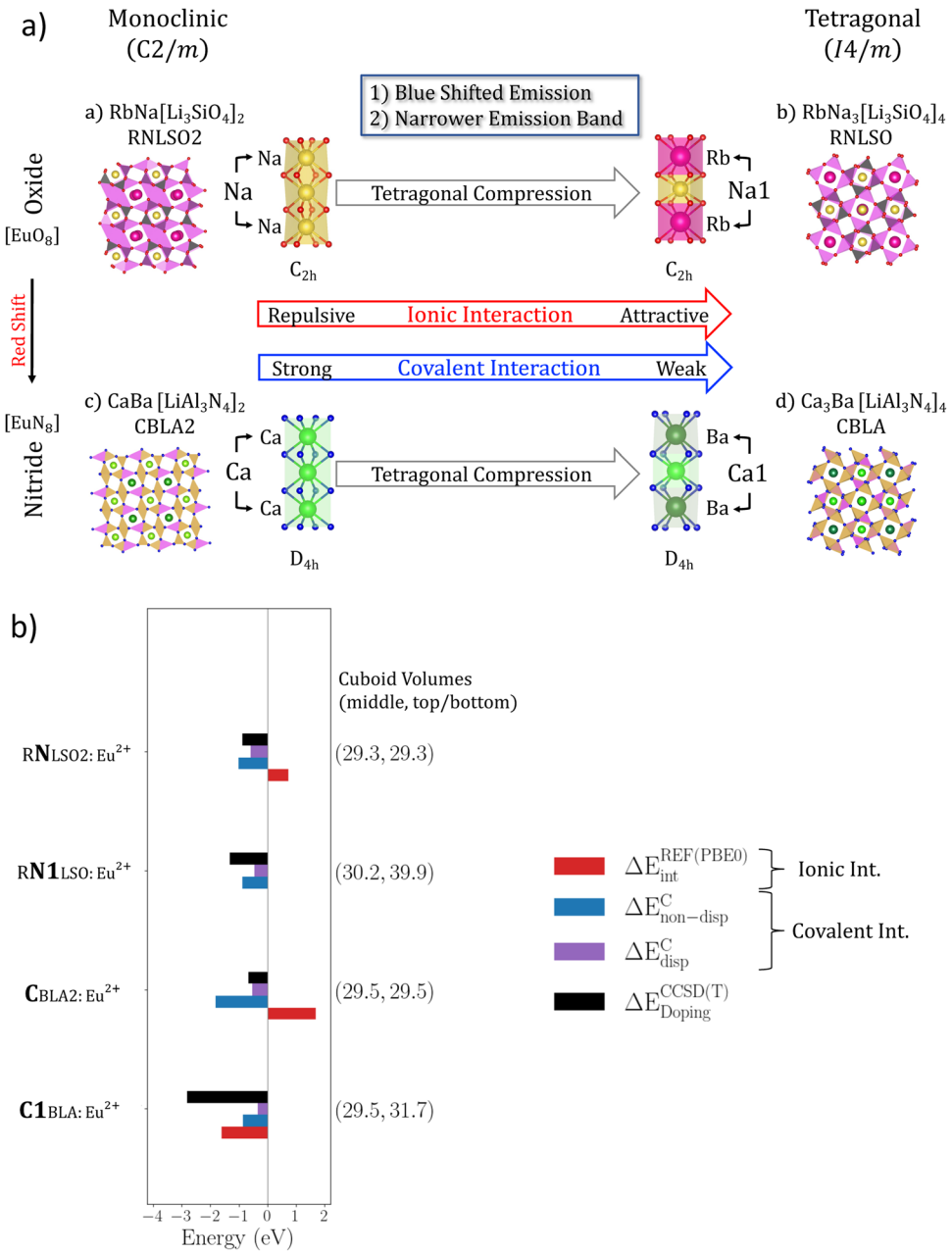

Fig. 7 (a) The impact of the tetragonal cuboid compression of the Na^+ and Ca^{2+} Eu^{2+}-doping centers in RNLSO2 and CBLA2 towards RNLSO and the isotypic CBLA phosphors. (b) Analysis of the DLPNO-CCSD(T) computed probability for Eu^{2+}-doping in these phosphors on the basis of ionic and covalent Eu^{2+}-host interactions in the framework of local energy decomposition (LED).

neutral ionic interaction (+0.02 eV) with the $[O_8Li_8Rb_2]^{6-}$ host coordination environment and slightly reduced covalent interactions. This is also reflected to the EuO_8 cuboid volumes and Eu–O bond distances (29.3 Å^3, 2.6 Å in RNLSO2 and 30.2 Å^3, 2.7 Å in RNLSO). Overall, the analysis confirms the improvement in the doping probability at the $Na(1)^+$ centers of RNLSO with respect to the Na^+ centers in RNLSO2. While the EuO_8 cuboid expansion and the covalency reduction along this direction are also consistent with the blue shifted and narrower bandwidth emission signal in RNLSO in comparison to RLNSO2 for these doped centers. We would like to emphasize that while within the local energy decomposition (LED) framework, the covalent interactions are probed in the ground state, it has been shown that the open Eu^{2+} $4f^7$ shell is only marginally involved in the bonding,[112] and the important covalent interactions with the host environment are actually taking place in the Eu^{2+} 5d and 6s shells. In this concept, these interactions are probing indirectly the bonding characteristics of the excited emissive states of the $4f^75d^1$ shell.

Na^+ and Rb^+ sites in RNLSO2 resemble the characteristics of the Ca^{2+} and Ba^{2+}sites in CBLA2. As shown in Fig. S7 (ESI†), Eu^{2+} doping at the respective Rb^+ and Ba^{2+} sites in RNLSO2 and CBLA2 leads to favorable doping situations. This is reflected in both the ionic and covalent interactions between the Eu^{2+} site and the host environment. Due to the negatively charged host environments, $[O_8Li_8Na_2]^{6-}$ and $[N_8Al_4Li_4Ba_2]^{4-}$ the Eu^{2+} site – host environment ionic interactions are attractive (2.7 and 2.3 eV) while the EuO_8 and EuN_8 cuboid expansions (Eu–O $\sim$ 3.00 Å and 40.5 Å^3 cuboid volume and Eu–N $\sim$ 2.93 A and 37.6 A^3 cuboid volume, respectively) lead to weaker covalent interactions, hence to weaker vibronic coupling at these sites, which is also reflected in the reduction of the emission bandwidths in comparison to the emission spectra originating from the respective Eu^{2+}-doped Na^+ and Ca^{2+} sites.

Likewise to the Rb^+ and Ba^{2+} sites, Eu^{2+} doping at Na^+ and Ca^{2+} in RNLSO2 and CBLA2 phosphors not only results in compressed EuO_8 and EuN_8 cuboids with similar principle emission characteristics with respect to the non-bonding Eu $5d_{x^2-y^2}$ MO character of the emissive state but also in terms of their probabilities for Eu^{2+} doping (Fig. 7 and Table S4, ESI†). As shown in Fig. 7a and b, both the Na^+ sites in RNLSO2 and the Ca^{2+} sites in CBLA2 are less favorable for Eu^{2+} doping showing significant repulsive ionic (+1.7 eV) interactions owning to the positive $[N_8Al_8Ca_2]^{4+}$ coordination environment opposing the rather covalent Eu^{2+}-host interactions (−2.4 eV). Hence as in the case of RNLSO2, at the Eu^{2+}-doped Na^+ sites, in the case of CBLA2, the overall doping probability, for the Eu^{2+}-doped Ca^{2+} sites is significantly reduced.

These results confirm the experimental and computational observations that for the RNLSO2:Eu^{2+} phosphor, the emission band characteristics can be improved by tuning the excitation laser to higher energies to basically probe the emission originating from Eu^{2+}-doped Rb^+ over Na^+ sites. Alternatively one may resort to the RNLSO:Eu^{2+} phosphor to benefit from the improved doping probability of the Eu^{2+}doped $Na(1)^+$ sites towards a unique, narrow band blue shifted emission band in comparison to the Eu^{2+}doped $Na(1)^+$ sites of RNLSO2:Eu^{2+}. In contrast in the case of CBLA2:Eu^{2+} phosphor, the only possibility to reduce the emission intensity losses into the IR is to in principle reduced the Eu^{2+} doping concentration to suppress the emission from the low probability for Eu^{2+} doping at Ca^{2+} centers at the cost of reducing the total light intensity and brightness of the phosphor. Hence, at this point, the question arises whether it is possible to alter the unfavorable emission characteristics of the CBLA2:Eu^{2+} phosphor by generating the hypothetical CBLA:Eu^{2+}doped phosphor that is isotypic to the RNLSO:Eu^{2+} phosphor. The structural characteristics of the hypothetical CBLA:Eu^{2+} doped phosphor are provided in the ESI† (Fig. S16, Section SV).

As shown in Fig. 7a and b likewise to the $Na(1)^+$ centers of RNLSO, the $Ca(1)^{2+}$ centers in CBLA form tetragonally compressed ($Ca^{2+}N_8$) cuboids owing to the formation of the asymmetric Ba^{2+}–$Ca(1)^{2+}$–Ba^{2+} cuboid sequence. In contrast to the Eu^{2+}-doped Ca^{2+} sites in CBLA2:Eu^{2+},Eu^{2+} doping at $Ca(1)^{2+}$ centers becomes favorable. This is due to the attractive ionic interactions between Eu^{2+} and $[N_8Al_8Ba_2]^{4+}$ host environment and the reduced covalent interactions leading to an improved probability for Eu^{2+} doping at these sites. The $Eu^{2+}N_8$ expansion (Eu–N, volume) and the suppression of the Eu host covalent interactions could in fact lead to a blue shifted narrow band emission signal in comparison to the Ca^{2+} Eu^{2+}-doped positions. However, as in fact shown in Table S4 and Fig. S7 (ESI†) in CBLA:Eu^{2+}, the doping probability of both $Ca(1)^{2+}$, $Ca2^{2+}$ and Ba^{2+} in comparison to the respective Ca^{2+} and Ba^{2+} Eu^{2+}-doped centers in CBLA2:Eu^{2+}, improves. The extent to which this could ultimately lead to a candidate phosphor with improved emission properties is investigated below.

3. CBLA is an 'ideal' hypothetical host for a red Eu-doped phosphor with extraordinary emission properties

Seeking further validation for the structural factors that could lead to a hypothetical candidate CBLA:Eu^{2+} phosphor with optimum emission properties, we analyze the vibronic coupling effect on the known CBLA2, RNLSO and RNLSO2 phosphors. At this point as shown schematically in Fig. S12 (ESI†), it is useful to recall that in 'ideal' cubic symmetry (inverted O_h) EuL_8 (L = O, N) cuboid, the emissive $^8T_{2g}$ is subject to the pseudo Jahn Teller (PJTE) effect towards tetragonally distorted cuboids (elongated or compressed along the 4-fold symmetry axis) leading to D_{4h} symmetry through coupling with e_g vibrational modes. In practice, for example in the presence of more than one cuboid, the situation is more complex as coupling with the respective t_{2g} is enabled, leading to a series of ($T_{2g}(e_g + t_{2g})$) PEJT along the tetragonal distortion pathway.

As discussed in Section II, in the case of CBLA2 Eu doping at Ba^{2+} centers results in tetragonally elongated EuN_8 cuboids with a volume of 37.5 Å^3 surrounded by tetragonally elongated BaN_8 cuboids of the same volume while doping at Ca^{2+} centers results in tetragonally compressed EuN_8 cuboids with a volume of 29.5 Å^3 surrounded by tetragonally compressed CaN_8 cuboids of the same volume. Along the list of vibrational modes that influence the emission bands in CBLA2 according to their

computed Huang–Rhys factors S,[102,103] the e_g group of vibrational modes, illustrated in Fig. S13 and S14a (ESI†), shows the most significant contributions. Not surprisingly, these group of modes represent the tetragonal distortion pathway of EuN_8, BaN_8 and CaN_8 cuboids. The DLPNO-CCSD(T) potential energy surface (PES) was computed as well as the respective emission spectra along the tetragonal distortion pathway at both Ba^{2+} and Ca^{2+} doping centers. The results are summarized in Fig. 8a and b and Fig. S14 (ESI†).

As seen in Fig. S14 (ESI†), at the Ba doping centers, both the EuN_8 cuboids at the doped Ba^{2+} center and the BaN_8 cuboids of the undoped centers maintain practically similar cuboid volumes along the tetragonal distortion pathway ($\sim$37 Å^3 at Q = 0 and $\sim$33 Å^3 at Q = 6). In contrast, at the Ca doping centers, the EuN_8 cuboid compresses further (from 29.5 Å^3 to 28.85 Å^3) while the CaN_8 ones expand (from 30.5 Å^3 at Q = 0 to 37.3 Å^3 at Q = 6). A similar trend is observed in the computed emission spectra shown in both Fig. S14 (ESI†) and Fig. 8b. In fact, along the compression pathway the emission arising from Eu^{2+}-doped Ba^{2+}centers, remains unaffected in terms of energy position and absolute intensity the respective emission band, arising from Eu^{2+}-doped Ca^{2+} centers, becomes blue-shifted with increasing intensity. Along the tetragonal distortion pathway, at normal mode value Q = 3, this band actually overtakes the total intensity while Q = 6 dominates the emission signal providing a unique red emission band at $\sim$14 300 cm^{-1}. It becomes evident that structural modifications that could stabilize the Eu^{2+}-doped centers around the Q = 6 magnitude of the axial compression pathway would potentially lead to an unprecedented narrow band red-emitting phosphor.

Hence in a next step at the trimer model CBLA2:Eu^2 structures containing Ca^{2+} doping centers, we exchange the Ca^{2+} undoped centers with Ba^{2+} in order to better accommodate the MN_8 (M = Ca^{2+}, Ba^{2+}) expansion along the EuN_8 compression pathway. Likewise, at the trimer structures that contain Ba^{2+} doping centers, we exchange the bulky Ba^{2+} centers with the smaller Ca^{2+} centers in an effort to minimize any remaining geometric strain at the CaN_8 cuboids along the EuN_8 compression pathway. In this way, the host cuboid asymmetric sequences Ba^{2+}–Ca^{2+}–Ba^{2+} and Ca^{2+}–Ba^{2+}–Ca^{2+} that are actually present in CBLA are formed. This is shown in Fig. S15, ESI.† As expected, this structural modification creates an asymmetry at the doped Ca^{2+} and Ba^{2+} sites in both the doped EuN_8 cuboids (35.8 Å^3 at Ca^{2+} site, 43.7 Å^3 at Ba^{2+} site) and undoped BaN_8 cuboids (33.2 Å^3 at Ca^{2+} site) and CaN_8 cuboids (32.4 Å^3 at Ba^{2+} site) at the formal CBLA2:Eu^{2+} equilibrium structure ($Q \sim 0$). This further reduces the local cuboid symmetries from D_{4h} to C_{2h} and activates a combination of e_g and t_{2g} modes that lead the tetragonal distortion. Allowing the system to relax along the tetragonally compression pathway, we compute once again the relevant PES of the CBLA:Eu^{2+} model.

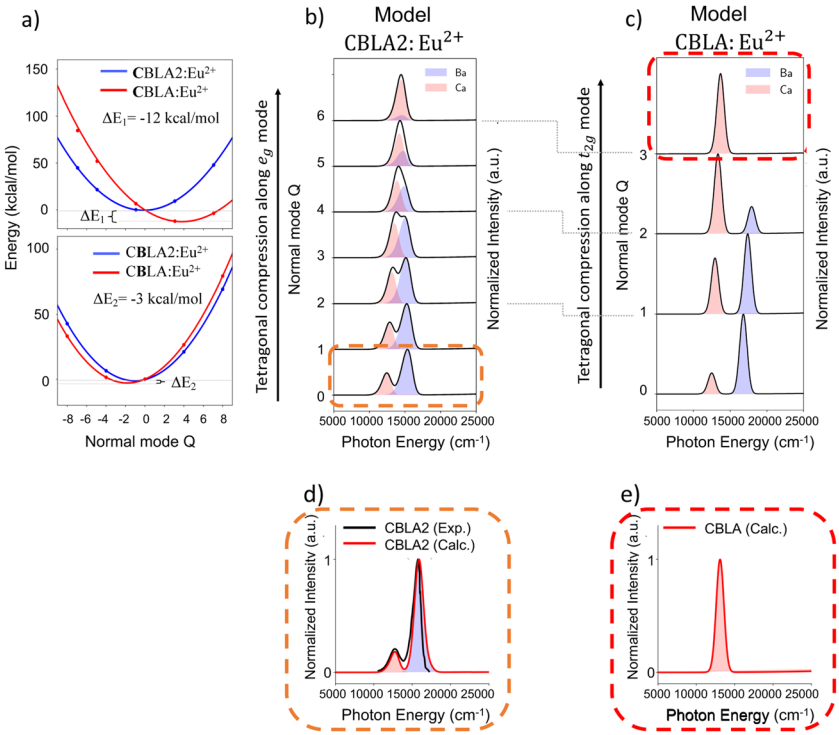

Fig. 8 (a) DLPNO-CCSD(T) PES of the CBLA2:Eu^{2+} and CBLA:Eu^{2+} model structures at both the Ca^{2+} and Ba^{2+} doping centers, along the respective e_g and t_{2g} tetragonally distorted pathways. (b) ESD/TDDFT/PBE0 computed emission spectra of the CBLA2:Eu^{2+} model along the e_g tetragonal distortion pathway. (c) ESD/TDDFT/PBE0 computed emission spectra of the CBLA:Eu^{2+} model structure along the respective t_{2g} tetragonal distortion pathway. (d) Experimental (black) and total ESD/TDDFT/PBE0 calculated (blue) emission spectra of CBLA^2:Eu^{2+} of two possible doping sites (Ca^{2+} and Ba^{2+}). (e) The red line corresponds to the calculated total emission spectrum of CBLA:Eu^{2+} of all possible doping centers ($Ca(1)^{2+}$, Ba^{2+} and $Ca(2)^{2+}$), where in practice Eu^{2+}-doped at Ba^{2+} and/or $Ca(2)^{2+}$ sites provide no intensity contributions to the total intensity.

In order to be able to compare the energetics between the CBLA2:Eu^{2+} and CBLA:Eu^{2+} PESs, the CBLA:Eu^{2+} is constructed on the basis of the CBLA2:Eu^{2+} $\overset{-2Ca}{\underset{+2Ba}{\longrightarrow}}$ CBLA:Eu^{2+} and CBLA2:Eu^{2+} $\overset{-2Ba}{\underset{+2Ca}{\longrightarrow}}$ CBLA:Eu^{2+} transformations at the Ca^{2+} and Ba^{2+} doping centers, respectively. As seen in Fig. 8a at the Ca^{2+}, Eu^{2+}-doped site, the CBLA:Eu^{2+} PES in comparison to the CBLA2:Eu^{2+} PES stabilizes at Q = 3 at about 12 kcal mol^{-1} indicating that along the tetragonal distortion pathway, the transformation of CBLA2:Eu^{2+} to CBLA:Eu^{2+} is energetically feasible. In contrast, no significant stabilization is observed of the CBLA:Eu^{2+} over the CBLA2:Eu^{2+} at the Eu^{2+}-doped Ba^{2+} centers. The relevant computed emission spectra are provided at Fig. 8c and Fig. S15 (ESI†). Interestingly, the intensity overtake at the Eu^{2+}-doped Ca^{2+} centers takes place already at Q = 2, in comparison to model CBLA2:Eu^{2+} (Q = 4), and at Q = 3, the emission is dominated by the Eu^{2+}-doped Ca^{2+} centers showing a red emission band at 14 700 cm^{-1}. The respective emission band corresponding to the Eu^{2+}-doped Ba^{2+} centers is shifted to higher energies and loses practically its intensity at Q = 3.

To summarize, the structural modifications that are necessary to transform CBLA2:Eu^{2+} phosphor to a unique narrow band red emitting phosphor require the presence of a hypothetical host with (1) containing an asymmetric sequence of cuboids around the Ca and Ba doping centers. For example, sequences of cuboids with Ba^{2+}–Ca^{2+}–Ba^{2+} and Ca^{2+}–Ba^{2+}–Ca^{2+} building units and (2) formation of EuN_8 cuboids so that the Eu $4f_{xyz}$ ↔ Eu $5d_{x^2-y^2}$ electron decay represents dipole allowed processes.

Looking into the structural characteristics of the isotypic CBLA2, RNLSO2 and RNLSO, we demonstrated in the previous sections that formation of the $Ca_3Ba[LiAl_3N_4]_4$:Eu^{2+}, CBLA host structure that is isotypic to RNLSO adopting the tetragonal ($I4/m$) space group fulfils the above structural requirements (Fig. S16, ESI†).

In fact as seen in Fig. S17a (ESI†), in the hypothetical CBLA:Eu^{2+} compound, Ca^{2+} and Ba^{2+} are alternating in the same channel forming cuboid sequences with $Ca(1)^{2+}$–Ba^{2+}–$Ca(1)^{2+}$–Ba^{2+} with elongated and compressed central cation BaN_8 and $Ca(1)N_8$ cuboids as well as $Ca(2)^{2+}$–$Ca(2)^{2+}$–$Ca(2)^{2+}$ ones with elongated $Ca(2)N_8$ cuboids. As shown in Table S4 (ESI†), all these doping positions are in principle available for Eu doping. As expected, the computed absorption spectrum shows distinct energy separation (~0.5 eV) between local (4f–5d) and metal to ligand charge transfer (MLCT) bands resulting in a potentially thermally stable Eu doped phosphor. According to the NTO analysis at the Eu^{2+}-doped $Ca(1)^{2+}$centers, emission from the C_{2h} symmetric (distorted D_{4h}) compressed EuN_8 cuboid is dominated by allowed Eu $4f_{xyz}$ ↔ Eu $5d_{x^2-y^2}$ electron decays, while at Ba and Ca(2) doped centers, emission from elongated EuN_8 cuboid (of approximately D_{4h} symmetry) emission is dominated by forbidden Eu $4f_{xyz}$ ↔ Eu $5d_{z^2}$ electron decays.

Collectively, as seen in (Fig. 8d, e and Fig. S17c, ESI†) and according to the expectations from the descriptor relationships (Fig. S11 and Table S5, ESI†), the computed emission spectrum of the hypothetical CBLA:Eu^{2+} is characterized by a single narrow red band with FWHM 1170 cm^{-1} (56 nm) at 14 800 cm^{-1} originating by the Eu^{2+}-doped $Ca(1)^{2+}$ centers. In this concept, CBLA:Eu^{2+} can be seen as a candidate derivative of CBLA2:Eu^{2+} with considerably improved photoluminescence properties. However, all the above require confirmation from the actual synthesis of CBLA:Eu^{2+} phosphors. We believe that the present study serves as an example of how systematic computational chemistry can be used to aid the synthetic efforts towards novel phosphor materials.

VII. Conclusions

A previously designed computational protocol for the color and the bandwidth prediction of narrow band phosphors[1] was extended to Eu^{2+}-doped phosphors containing multiple probable centers for Eu^{2+} doping. Namely, the narrow-band phosphors (Ca/Ba) nitridolithoaluminate $CaBa[LiAl_3N_4]_2$:Eu^{2+} (CBLA2),[38] alkali (Na/Rb) lithosilicate $RbNa_3[Li_3SiO_4]_4$:Eu^{2+} (RNLSO)[52] and $RbNa[Li_3SiO_4]_2$:Eu^{2+} (RNLSO2)[53] phosphors. In particular, a non-standard computational strategy was employed in an effort to develop the information content that connects the geometric and electronic structure characteristics of these phosphors with their emission properties with an ultimate goal to systematically improve the emission losses into the IR region of the CBLA2 phosphor towards a novel phosphor material that synthesized *in silico*, best resembles the geometric characteristics of the hypothetical $Ca_3Ba[LiAl_3N_4]_4$:Eu^{2+} (CBLA) phosphor and shows unprecedented narrow band red emission characteristics. Following a thorough electronic structure analysis, converged embedded cluster structures were constructed for the variety of the Eu^{2+}-doped positions (Ca^{2+}, Ba^{2+}, Na^+ or Rb^+) across the study set of phosphors. In the following the different probable doping positions were computed at the DLPNO-CCSD(T) level of theory while TD/DFT in conjunction with excited state dynamics was employed to compute the excited state properties.

In particular, it was shown that the most probable doping centers are those enabling the formation of relaxed EuL_8 cuboids dictating the Ba^{2+} and Rb^+ positions as the most probable positions for Eu^{2+}-doping in the case of CBLA2, and (RNLSO and RNLSO2) phosphors. In this concept, the absorption and luminescence spectra of the chosen study set of phosphors were computed, on the basis of the defined doping and symmetry selection rules, showing very good agreement with the experimental results. Once again,[1] it was shown that the suppression of the Eu–O/N covalent interactions, as well as the steric effects imposed by the second coordination sphere, is the origin of the desired narrow band emission across the most probable centers for Eu^{2+}doping.

This analysis led us to realize that the Na^+ and Rb^+ sites in RNLSO2 resemble the geometric and electronic structure characteristics of the Ca^{2+} and Ba^{2+}sites in CBLA2. Most importantly, it was shown that Eu^{2+}-doping of the $Na(1)^+$ sites in

RNLSO is more favorable than the Eu^{2+} doping of the Na^{+} sites in RNLSO2 leading to improved emission characteristics as the origin of the blue shifted, single narrow band emission spectrum in the former.[52,53]

This inspired us to synthesize, *in silico*, the respective CBLA phosphor with an ultimate goal to improve the emission characteristics of the Ca^{2+} sites in CBLA2. It was indeed demonstrated that the geometric transformation of CBLA2 to CBLA follows a tetragonal cuboid compression pathway along the most important coupling vibrational modes dominating the emission bands in CBLA2. The resulted CBLA phosphor host environment that is involved in the Eu^{2+}-doping process is more feasible energetically. It creates a host environment which renders the emission from the relevant $Ca(1)^{2+}$ Eu^{2+} doped sites a favorable process leading to a blue shifted narrow band red emission signal in comparison to the Ca^{2+} Eu^{2+}-doped sites in CBLA2. At the same time, emission from the $Ca(2)^{2+}$ and Ba^{2+} Eu^{2+}-doped sites is negligible due to symmetry reasons. Overall, this resulted in a single narrow band red emission, that is computationally predicted at around 14 800 cm^{-1} and FWHM 1170 cm^{-1}, introducing the CBLA as a candidate phosphor with potentially unprecedented emission properties for pc-LEDs applications.

We believe that the results presented herein are important in the design of novel narrow band phosphors with tunable emission properties and for further improving the quality and the energy efficiency of phosphor converted LEDs. In this direction, research is ongoing in our laboratories to validate the concept of the computational predictions by synthesizing candidate phosphors of the novel CBLA phosphor family, for predicting the potential photoluminescence properties of other yet unknown promising phosphor materials, as well as for a general and in depth understanding of the narrow band emission mechanisms.

Conflicts of interest

There are no conflicts to declare.

Acknowledgements

F. N., D. M., and R. S. would like to thank the Max Planck Society for financial support. F. N., D. M. and W. S. acknowledge funding support from the Deutsche Forschungsgemeinschaft (DFG, German Research Foundation) under Germany's Excellence Strategy-EXC 2089/1-390776260 (e-conversion). R. S. would like to thank the Egyptian Ministry of Higher Education and Scientific Research for financial support. Open Access funding provided by the Max Planck Society.

References

1 R. Shafei, D. Maganas, P. J. Strobel, P. J. Schmidt, W. Schnick and F. Neese, *J. Am. Chem. Soc.*, 2022, **144**, 8038–8053.
2 M.-H. Fang, Z. Bao, W.-T. Huang and R.-S. Liu, *Chem. Rev.*, 2022, **122**, 11474–11513.
3 M.-H. Fang, C. O. M. Mariano, P.-Y. Chen, S.-F. Hu and R.-S. Liu, *Chem. Mater.*, 2020, **32**, 1748–1759.
4 J. L. Leaño, M.-H. Fang and R.-S. Liu, *ECS J. Solid State Chem. Tech.*, 2017, **7**, R3111–R3133.
5 N. D. Q. Anh, P. X. Le and H.-Y. Lee, *Curr. Opt. Photonics*, 2019, **3**, 78–85.
6 Y. N. Ahn, K. D. Kim, G. Anoop, G. S. Kim and J. S. Yoo, *Sci. Rep.*, 2019, **9**, 16848.
7 S. A. Khan, N. Z. Khan, M. Sohail, J. Ahmed, N. Alhokbany, S. M. Alshehri, X. Xu, J. Zhu and S. Agathopoulos, *J. Mater. Chem. C*, 2021, **9**, 13041–13071.
8 L. Wang, X. Wang, T. Kohsei, K. I. Yoshimura, M. Izumi, N. Hirosaki and R. J. Xie, *Opt. Express*, 2015, **23**, 28707.
9 M. Zhao, Q. Zhang and Z. Xia, *Mater. Today*, 2020, **40**, 246–265.
10 T. Walther and E. S. Fry, *Optics in Our Time*, Springer, Cham, 2016, pp. 201–222.
11 S. Li, R.-J. Xie, T. Takeda and N. Hirosaki, *ECS J. Solid State Chem. Tech.*, 2017, **7**, R3064–R3078.
12 R.-J. Xie, Y. Q. Li, N. Hirosaki and H. Yamamoto, *Nitride phosphors and solid-state lighting*, Taylor & Francis, Boca Raton, FL, 2011.
13 Y. Wang, Z. Wang, G. Wei, Y. Yang, S. He, J. Li, Y. Shi, R. Li, H. Suo and P. Li, *Opt. Express*, 2022, **30**, 28550–28558.
14 H. Xiao, J. Zhang, L. Zhang, H. Wu, H. Wu, G. Pan, F. Liu and J. Zhang, *Adv. Opt. Mater.*, 2021, **9**, 2101134.
15 S. Saikia, A. Joshi, H. Arfin, S. Badola, S. Saha and A. Nag, *Angew. Chem., Int. Ed.*, 2022, **61**, e202201628.
16 P. Strobel, C. Maak, V. Weiler, P. J. Schmidt and W. Schnick, *Angew. Chem., Int. Ed.*, 2018, **57**, 8739–8743.
17 K. Uheda, N. Hirosaki, Y. Yamamoto, A. Naito, T. Nakajima and H. Yamamoto, *Electrochem. Solid-State Lett.*, 2006, **9**, H22.
18 E. F. Schubert and J. K. Kim, *Science*, 2005, **308**, 1274.
19 S. Pimputkar, J. S. Speck, S. P. DenBaars and S. Nakamura, *Nat. Photonics*, 2009, **3**, 180–182.
20 Y. Zhuo, A. Mansouri Tehrani, A. O. Oliynyk, A. C. Duke and J. Brgoch, *Nat. Commun.*, 2018, **9**, 4377.
21 Z. Wang, I.-H. Chu, F. Zhou and S. P. Ong, *Chem. Mater.*, 2016, **28**, 4024–4031.
22 S. Schmiechen, P. Strobel, C. Hecht, T. Reith, M. Siegert, P. J. Schmidt, P. Huppertz, D. Wiechert and W. Schnick, *Chem. Mater.*, 2015, **27**, 1780–1785.
23 P. Pust, V. Weiler, C. Hecht, A. Tücks, A. S. Wochnik, A.-K. Henß, D. Wiechert, C. Scheu, P. J. Schmidt and W. Schnick, *Nat. Mater.*, 2014, **13**, 891–896.
24 T. M. Tolhurst, S. Schmiechen, P. Pust, P. J. Schmidt, W. Schnick and A. Moewes, *Adv. Opt. Mater.*, 2016, **4**, 584–591.
25 T. M. Tolhurst, T. D. Boyko, P. Pust, N. W. Johnson, W. Schnick and A. Moewes, *Adv. Opt. Mater.*, 2015, **3**, 546.
26 S. Schmiechen, H. Schneider, P. Wagatha, C. Hecht, P. J. Schmidt and W. Schnick, *Chem. Mater.*, 2014, **26**, 2712–2719.

27 M. Zeuner, F. Hintze and W. Schnick, *Chem. Mater.*, 2009, **21**, 336.
28 C. Hecht, F. Stadler, P. J. Schmidt, J. S. auf der Günne, V. Baumann and W. Schnick, *Chem. Mater.*, 2009, **21**, 1595.
29 R. Mueller-Mach, G. Mueller, M. R. Krames, H. A. Höppe, F. Stadler, W. Schnick, T. Juestel and P. Schmidt, *Phys. Status Solidi A*, 2005, **202**, 1727–1732.
30 M. Zhao, H. Liao, M. S. Molokeev, Y. Zhou, Q. Zhang, Q. Liu and Z. Xia, *Light: Sci. Appl.*, 2019, **8**, 38.
31 T. M. Tolhurst, P. Strobel, P. J. Schmidt, W. Schnick and A. Moewes, *Chem. Mater.*, 2017, **29**, 7976–7983.
32 M. Zhao, Z. Yang, L. Ning and Z. Xia, *Adv. Mater.*, 2021, **33**, e2101428.
33 F. Ruegenberg, M. Seibald, D. Baumann, S. Peschke, F. Philipp and H. Huppertz, *Chemistry*, 2021, **27**, 11701–11706.
34 D. S. Wimmer, M. Seibald, D. Baumann, S. Peschke, K. Wurst, G. Heymann, D. Dutzler, A. Garcia-Fuente, W. Urland and H. Huppertz, *Eur. J. Inorg. Chem.*, 2021, 4470–4481.
35 F. Ruegenberg, A. García-Fuente, M. Seibald, D. Baumann, S. Peschke, W. Urland, A. Meijerink, H. Huppertz and M. Suta, *Adv. Opt. Mater.*, 2021, **9**, 2101643.
36 M. Liao, Q. Wang, Q. Lin, M. Xiong, X. Zhang, H. Dong, Z. Lin, M. Wen, D. Zhu, Z. Mu and F. Wu, *Adv. Opt. Mater.*, 2021, **9**, 2100465.
37 G. J. Hoerder, M. Seibald, D. Baumann, T. Schroder, S. Peschke, P. C. Schmid, T. Tyborski, P. Pust, I. Stoll, M. Bergler, C. Patzig, S. Reissaus, M. Krause, L. Berthold, T. Hoche, D. Johrendt and H. Huppertz, *Nat. Commun.*, 2019, **10**, 1824.
38 P. Wagatha, V. Weiler, P. J. Schmidt and W. Schnick, *Chem. Mater.*, 2018, **30**, 7885–7891.
39 Y. Xie, T. Tian, C. Mao, Z. Wang, J. Shi, L. Yang and C. Wang, *Nanomaterials*, 2023, **13**, 599.
40 K. Singh, M. Rajendran, R. Devi and S. Vaidyanathan, *Inorg. Chem.*, 2022, **61**, 2768–2782.
41 W. Setyawan, R. M. Gaume, S. Lam, R. S. Feigelson and S. Curtarolo, *ACS Comb. Sci.*, 2011, **13**, 382.
42 C. J. Duan, X. J. Wang, W. M. Otten, A. C. A. Delsing, J. T. Zhao and H. T. Hintzen, *Chem. Mater.*, 2008, **20**, 1597.
43 C. M. Fang, H. T. Hintzen, G. D. With and R. A. D. Groot, *J. Phys.: Condens. Matter*, 2001, **13**, 67.
44 F. Ruegenberg, A. García-Fuente, M. Seibald, D. Baumann, G. Hoerder, T. Fiedler, W. Urland, H. Huppertz, A. Meijerink and M. Suta, *Adv. Opt. Mater.*, 2023, 2202732.
45 J. Bouquiaux, S. Poncé, Y. Jia, A. Miglio, M. Mikami and X. Gonze, *Adv. Opt. Mater.*, 2021, **9**, 2100649.
46 J. Brgoch, S. P. DenBaars and R. Seshadri, *J. Phys. Chem. C*, 2013, **117**, 17955.
47 G. Hautier, A. Jain, S. P. Ong, B. Kang, C. Moore, R. Doe and G. Ceder, *Chem. Mater.*, 2011, **23**, 3495.
48 S. P. Ong, L. Wang, B. Kang and G. Ceder, *Chem. Mater.*, 2008, **20**, 1798.
49 G. Kresse and J. Furthmüller, *Phys. Rev. B: Condens. Matter Mater. Phys.*, 1996, **54**, 11169.
50 Y. Zhuo, A. Mansouri Tehrani and J. Brgoch, *J. Phys. Chem. Let.*, 2018, **9**, 1668–1673.
51 P. Pust, A. S. Wochnik, E. Baumann, P. J. Schmidt, D. Wiechert, C. Scheu and W. Schnick, *Chem. Mater.*, 2014, **26**, 3544–3549.
52 H. Liao, M. Zhao, M. S. Molokeev, Q. Liu and Z. Xia, *Angew. Chem., Int. Ed.*, 2018, **57**, 11728–11731.
53 M. Liao, Z. Mu, Q. Wang, X. Zhang, H. Dong, M. Wen and F. Wu, *J. Alloys Compd.*, 2020, **837**, 11728–11731.
54 S. Lai, M. Zhao, Y. Zhao, M. S. Molokeev and Z. Xia, *ACS Mater. Au*, 2022, **2**, 374–380.
55 X. Wang, X. Huang, M. Zhao, P. A. Tanner, X. Zhou and L. Ning, *Inorg. Chem.*, 2022, **61**, 7617–7623.
56 T. Jansen, J. Gorobez, M. Kirm, M. G. Brik, S. Vielhauer, M. Oja, N. M. Khaidukov, V. N. Makhov and T. Jüstel, *ECS J. Solid State Chem. Tech.*, 2018, **7**, R3086.
57 W. Zhou, Y. Ou, L. Huang, E. Song, F. Ma, Z. Xia, H. Liang and Q. Zhang, *Adv. Mater.*, 2022, **34**, 2206278.
58 J. Bouquiaux, S. Poncé, Y. Jia, A. Miglio, M. Mikami and X. Gonze, *Chem. Mater.*, 2023, 5353–5361.
59 J. Xu, X. Huang, X. Cheng, M.-H. Whangbo and S. Deng, *Angew. Chem., Int. Ed.*, 2022, **61**, e202116404.
60 R. D. Shannon, *Acta Crystallogr., Sect. A: Found. Crystallogr.*, 1976, **32**, 751–767.
61 F. Neese, *Wiley Interdiscip. Rev.: Comput. Mol. Sci.*, 2012, **2**, 73–78.
62 F. Neese, *Wiley Interdiscip. Rev.: Comput. Mol. Sci.*, 2018, **8**, e1327.
63 F. Neese, F. Wennmohs, U. Becker and C. Riplinger, *J. Chem. Phys.*, 2020, **152**, 224108.
64 F. Neese, *Wiley Interdiscip. Rev.: Comput. Mol. Sci.*, 2022, **12**, e1606.
65 A. Schäfer, H. Horn and R. Ahlrichs, *J. Chem. Phys.*, 1992, **97**, 2571–2577.
66 F. Weigend and R. Ahlrichs, *Phys. Chem. Chem. Phys.*, 2005, **7**, 3297–3305.
67 D. A. Pantazis, X. Y. Chen, C. R. Landis and F. Neese, *J. Chem. Theory Comput.*, 2008, **4**, 908.
68 D. A. Pantazis and F. Neese, *J. Chem. Theory Comput.*, 2009, **5**, 2229.
69 D. A. Pantazis and F. Neese, *J. Chem. Theory Comput.*, 2011, **7**, 677.
70 D. A. Pantazis and F. Neese, *Theor. Chem. Acc.*, 2012, **131**, 1292.
71 K. Eichkorn, O. Treutler, H. Öhm, M. Häser and R. Ahlrichs, *Chem. Phys. Lett.*, 1995, **240**, 283–290.
72 F. Neese, F. Wennmohs, A. Hansen and U. Becker, *Chem. Phys.*, 2009, **356**, 98–109.
73 B. Helmich-Paris, B. de Souza, F. Neese and R. Izsák, *J. Chem. Phys.*, 2021, **155**, 104109.
74 M. Douglas and N. M. Kroll, *Ann. Phys.*, 1974, **82**, 89–155.
75 B. A. Hess, *Phys. Rev. A: At., Mol., Opt. Phys.*, 1986, **33**, 3742–3748.
76 L. Visscher and K. G. Dyall, *At. Data Nucl. Data Tables*, 1997, **67**, 207–224.
77 W. R. Wadt and P. J. Hay, *J. Chem. Phys.*, 1985, **82**, 284–298.
78 P. J. Hay and W. R. Wadt, *J. Chem. Phys.*, 1985, **82**, 270–283.
79 P. J. Hay and W. R. Wadt, *J. Chem. Phys.*, 1985, **82**, 299–310.

80 T. H. Dunning and P. J. Hay, in *Methods of Electronic Structure Theory*, ed. H. F. Schaefer, Springer US, Boston, MA, 1977, ch. 1, pp. 1–27.
81 O. Demel, J. Pittner and F. Neese, *J. Chem. Theory Comput.*, 2015, **11**, 3104–3114.
82 D. G. Liakos and F. Neese, *J. Chem. Theory Comput.*, 2015, **11**, 2137–2143.
83 A. Dreuw and M. Head-Gordon, *Chem. Rev.*, 2005, **105**, 4009–4037.
84 J. P. Perdew, K. Burke and Y. Wang, *Phys. Rev. B: Condens. Matter Mater. Phys.*, 1996, **54**, 16533.
85 C. Adamo and V. Barone, *J. Chem. Phys.*, 1999, **110**, 6158–6170.
86 J. P. Perdew, M. Ernzerhof and K. Burke, *J. Chem. Phys.*, 1996, **105**, 9982–9985.
87 J. P. Perdew, K. Burke and M. Ernzerhof, *Phys. Rev. Lett.*, 1996, **77**, 3865.
88 T. Yanai, D. P. Tew and N. C. Handy, *Chem. Phys. Lett.*, 2004, **393**, 51–57.
89 S. Grimme, *J. Chem. Phys.*, 2006, **124**, 034108.
90 M. Casanova-Páez, M. B. Dardis and L. Goerigk, *J. Chem. Theory Comput.*, 2019, **15**, 4735–4744.
91 B. O. Roos, P. R. Taylor and P. E. M. Siegbahn, *Chem. Phys.*, 1980, **48**, 157–173.
92 P. E. M. Siegbahn, J. Almlof, A. Heiberg and B. O. Roos, *J. Chem. Phys.*, 1981, **74**, 2384–2396.
93 C. Angeli, R. Cimiraglia, S. Evangelisti, T. Leininger and J. P. Malrieu, *J. Chem. Phys.*, 2001, **114**, 10252–10264.
94 C. Angeli and R. Cimiraglia, *Theor. Chem. Acc.*, 2002, **107**, 313–317.
95 C. Riplinger and F. Neese, *J. Chem. Phys.*, 2013, **138**, 034106.
96 Y. Guo, C. Riplinger, D. G. Liakos, U. Becker, M. Saitow and F. Neese, *J. Chem. Phys.*, 2020, **152**, 024116.
97 M. Saitow, U. Becker, C. Riplinger, E. F. Valeev and F. Neese, *J. Chem. Phys.*, 2017, **146**, 164105.
98 F. Neese, *J. Chem. Phys.*, 2005, **122**, 34107.
99 F. Neese, F. Wennmohs and A. Hansen, *J. Chem. Phys.*, 2009, **130**, 114108.
100 F. Neese, *J. Am. Chem. Soc.*, 2006, **128**, 10213–10222.
101 S. Hirata and M. Head-Gordon, *Chem. Phys. Lett.*, 1999, **314**, 291–299.
102 B. de Souza, G. Farias, F. Neese and R. Izsák, *J. Chem. Phys.*, 2019, **150**, 214102.
103 B. de Souza, G. Farias, F. Neese and R. Izsák, *J. Chem. Theory Comput.*, 2019, **15**, 1896–1904.
104 B. de Souza, F. Neese and R. Izsák, *J. Chem. Phys.*, 2018, **148**, 034104.
105 A. Dittmer, G. L. Stoychev, D. Maganas, A. A. Auer and F. Neese, *J. Chem. Theory Comput.*, 2020, **16**, 6950–6967.
106 A. Dittmer, R. Izsák, F. Neese and D. Maganas, *Inorg. Chem.*, 2019, **58**, 9303–9315.
107 A. Kubas, D. Berger, H. Oberhofer, D. Maganas, K. Reuter and F. Neese, *J. Phys. Chem. Let.*, 2016, **7**, 4207–4212.
108 D. Maganas, M. Roemelt, M. Havecker, A. Trunschke, A. Knop-Gericke, R. Schlogl and F. Neese, *Phys. Chem. Chem. Phys.*, 2013, **15**, 7260–7276.
109 R. Izsak, C. Riplinger, N. S. Blunt, B. de Souza, N. Holzmann, O. Crawford, J. Camps, F. Neese and P. Schopf, *J. Comput. Chem.*, 2023, **44**, 406–421.
110 Q. Lu, F. Neese and G. Bistoni, *Phys. Chem. Chem. Phys.*, 2019, **21**, 11569–11577.
111 A. Altun, M. Saitow, F. Neese and G. Bistoni, *J. Chem. Theory Comput.*, 2019, **15**, 1616–1632.
112 D. Aravena, M. Atanasov and F. Neese, *Inorg. Chem.*, 2016, **55**, 4457–4469.